Journal of Astronomical Telescopes, Instruments, and Systems

AstronomicalTelescopes.SPIEDigitalLibrary.org

10- to 19.5-GHz microwave receiver of an electro-optical interferometer for radio astronomy

Beatriz Aja
Luisa de la Fuente
Eduardo Artal
Enrique Villa
Juan L. Cano
Angel Mediavilla

SPIE.

Beatriz Aja, Luisa de la Fuente, Eduardo Artal, Enrique Villa, Juan L. Cano, Angel Mediavilla, "10- to 19.5-GHz microwave receiver of an electro-optical interferometer for radio astronomy," *J. Astron. Telesc. Instrum. Syst.* **5**(3), 035007 (2019), doi: 10.1117/1.JATIS.5.3.035007.

10- to 19.5-GHz microwave receiver of an electro-optical interferometer for radio astronomy

Beatriz Aja,[a,*] Luisa de la Fuente,[a] Eduardo Artal,[a] Enrique Villa,[b] Juan L. Cano,[a] and Angel Mediavilla[a]
[a]University of Cantabria, Department Communications Engineering, Santander, Spain
[b]Instituto de Astrofísica de Canarias, IACTec, La Laguna, Spain

Abstract. This document describes the analysis, design, and prototype test results of the microwave section of a 10- to 19.5-GHz interferometer, aimed at obtaining polarization data of cosmic microwave background (CMB) radiation from the sky. First, receiver analysis is thoroughly assessed to study the contribution of each subsystem when obtaining the Stokes parameters of an input signal. Then, the receiver design is detailed starting from the front-end module, which works at cryogenic temperature, composed of a set of passive components: feed-horn, orthomode transducer, and polarizer, together with active components, such as very low-noise amplifiers. The back-end module (BEM) is directly connected, working at room temperature for further amplification, phase switching, and correlation of the signals. Moreover, the whole frequency band is split into two sub-bands (10 to 14 GHz and 16 to 20 GHz) using a high selective diplexer in the BEM in order to reject radiofrequency interferences. Phase switches allow phase difference steps of 5.625 deg, which modulate the correlated outputs to reduce systematic effects in the postdetection signal processing. Finally, measurements of all the subsystems comprising the microwave section of the receiver as well as the characterization of the complete microwave receiver are presented. The obtained results demonstrate successful performance of the microwave receiver that, together with an electro-optical correlator and a near-infrared camera, comprises the interferometer. Moreover, synthesized images corresponding to combinations of the Stokes parameters can be obtained with the whole system. [DOI: 10.1117/1.JATIS.5.3.035007]

Keywords: interferometer; cosmic microwave background; Stokes parameters; radio astronomy; polarimeter.

Paper 19028 received Mar. 25, 2019; accepted for publication Jul. 30, 2019; published online Aug. 16, 2019.

1 Introduction

One of the main cosmological observables that give information regarding the early universe is the cosmic microwave background (CMB). Several experiments have been developed in the last years (ABS, BICEPS-2, EBEX, Keck Array, LSPE, POLARBEAR, QUBIC, QUIET, QUIJOTE, SPIDER, and Planck), trying to search for the primordial B-mode polarization signature.[1–3] Since CMB data are contaminated by astrophysical emissions associated with galactic and extragalactic sources, it is crucial to have information from a range of frequencies in order to distinguish these foregrounds from the cosmological signal based on their different spectral dependence. The success of future CMB polarization experiments involves the improved understanding and removal of foreground emissions from our own galaxy. Most of the observational efforts planned from ground experiments in the coming years are focused on frequencies around or above the minimum of the foreground emission and therefore, a detailed characterization of low-frequency foregrounds (synchrotron and anomalous microwave emission) is of great interest.[4] This information is key to clean the high-frequency maps from these contaminating signals and to unmask the underlying primordial B-mode signal.

Extremely sensitive receivers in radio astronomy are always increasingly in demand in order to improve the sensitivity of CMB experiments, whose goal is to get a better understanding of the early Universe.[5–8] In general, the instruments are broadband radiometers with their front-ends operated at cryogenic temperatures to reduce as much as possible the noise added by the subsequent stages. The polarization of the CMB signal can be measured using special radiometer configurations, acting as polarimetric receivers to finally obtain the Stokes parameters of the received CMB signal.[3,9–11]

On the other hand, radio interferometry is a particularly valuable technique for the study of the CMB anisotropy, due to its inherently high stability and robustness against many systematic errors.[12–14] Since the angular resolution is fixed by the size of the instrument in wavelengths, the system temperature and the instrument bandwidth determine the brightness sensitivity. Regarding the system temperature, amplifiers have been continuously reducing their noise contribution in such a way that the atmosphere and the passive elements in front of the cryogenic amplifier may be the dominant noise source, especially in ground-based instruments. Hence, widening bandwidth remains a good option to increase sensitivity.

The cross-correlator is one of the main parts of an interferometer, where the signals from each antenna are combined to form the complex visibility measurements to get the image of the sky. In those observations that require high sensitivity, analog correlators are preferred since digital counterparts have limited bandwidths and digitalization processes are avoided. Several analog lag-correlators have been presented in the literature when moderate spectral resolution is required.[15–17] Nevertheless, some measurements, like those involved in CMB state polarization, do not require spectral information and analog complex-correlators can be used to measure the Stokes

*Address all correspondence to Beatriz Aja, E-mail: beatriz.aja@unican.es

parameters.[18,19] When broadband input signals need to be correlated in a single channel, electro-optic correlators have shown some advantages over traditional analog ones.[20]

In order to improve the sensitivity, an interferometer with very sensitive receivers and an electro-optical correlator, which allows us to obtain a synthesized image of the Stokes parameters of the CMB polarization in the near-infrared (NIR), is proposed.[21] This improvement will be possible due to a substantial increment in the number of pixels as compared to the current image telescopes, as well as a lower complexity with respect to classical correlators. Moreover, an additional advantage of the proposed instrument is that it can be easily installed in observatories placed in the northern and southern hemispheres to obtain a complete sky coverage of the contaminant emissions, as is required for future space missions.

This paper presents the analysis, design, and characterization of the microwave receiver systems of an interferometer prototype working in the 10- to 19.5-GHz band. The selection of this frequency band will allow removal of the synchrotron emission and other contaminants, which dominate the low-frequency range of the spectrum and are also present at higher frequencies. The future experiments, including ground-based and on-board ones as well as a future space mission similar to COrE+,[22] are designed to operate with a wider range of frequencies, which is often insufficient for the proper characterization of those emissions.

This paper is set out in the following way: Sec. 2 describes the design of the complete interferometer. Section 3 presents a thorough analysis of the receiver for linearly polarized input signals. The design and performance of the microwave receiver are included in Sec. 4. System measurements are shown in Sec. 5. Finally, some conclusions are drawn in Sec. 6.

2 Interferometer Design

The architecture of the presented interferometer is shown in Fig. 1. The microwave system is depicted in blue, which is responsible for the separation of the two orthogonal electrical field components of the incoming wave as well as the amplification and filtering. Then, two frequency bands are defined: 10 to 14 GHz for the first band and 16 to 20 GHz for the second one, thus avoiding the interfering signals at 15 GHz present at the observatory location. Phase-switching modules are used to introduce a variable phase shift modulation between the two polarization components as well as for frequency band division. Moreover, a fast switching rate could be fast enough in order to overcome the level of $1/f$ noise of the receiver.

The advantage of the proposed interferometer consists of the phase switches, which allow a fast phase difference step of 5.625 deg, close to a continuous modulation. A 180 deg/90 deg modulation can be also applied as the instruments in Refs. 3, 10, and 11. A small discrete phase step leads to redundant information, and more accurate correction of systematic errors is expected. The measurement accuracy improvement against time-consuming with redundant states will be evaluated during the system integration with the electro-optical correlator and its characterization.

The outputs of each sub-band are correlated in microwave correlation modules, based on power dividers and 90 deg hybrids, in order to obtain four outputs to calculate the Stokes parameters simultaneously. Finally, these eight outputs (four for each receiver) are the inputs for an electro-optical correlator, which modulate a NIR laser using Mach–Zehnder modulators. The microwave receiver is designed to fulfill the required input power of the electro-optical correlator modulators. The NIR modulated signals are filtered and grouped in fiber bundles that

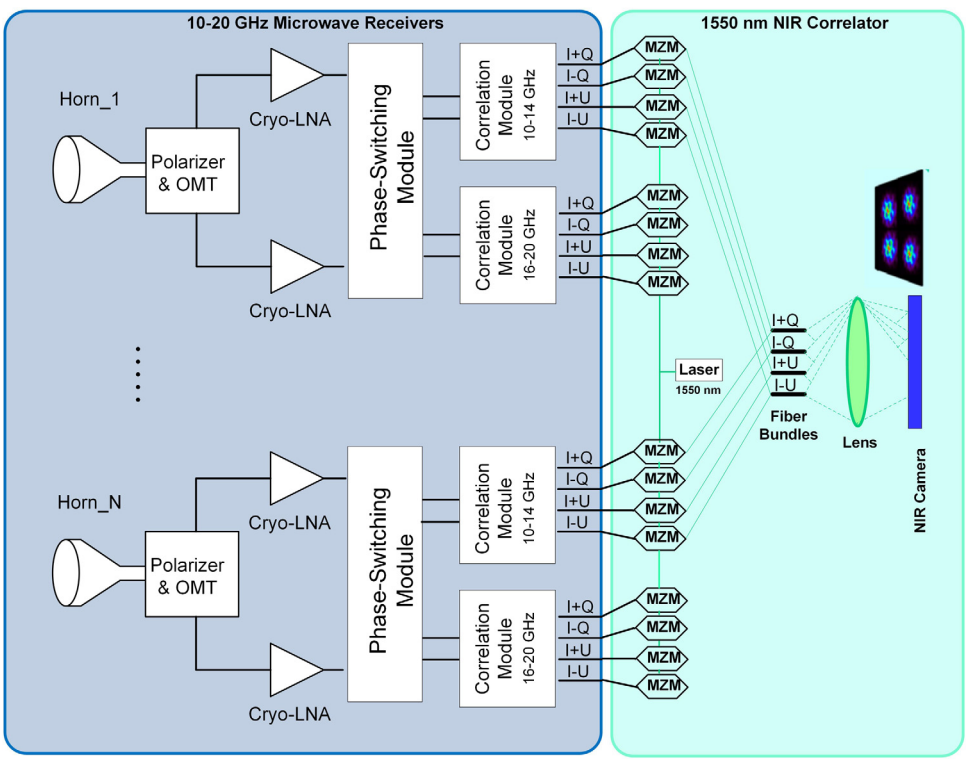

Fig. 1 Block diagram of the complete interferometer, with the microwave system in blue and the optical part in green.

illuminate the lens producing the interference. Finally, at the focal plane of this lens, a NIR camera is placed to have eight synthesized images corresponding to combinations of I, Q, and U parameters in the sub-bands previously defined by microwave diplexers.

3 Microwave Receiver Analysis

The interferometer covers the full frequency range from 10 to 19.5 GHz, and it is aimed at measuring the four Stokes parameters of a polarized incident wave.[23] For that purpose, the microwave receiver architecture is of great importance since it is designed to provide output signals whose combination is proportional to those Stokes parameters. The Stokes parameters in terms of two linear orthogonal electric field components in standard Cartesian basis $(\hat{x}, \hat{y})$ are defined as

$$I = \langle E_x^2 \rangle + \langle E_y^2 \rangle, \tag{1}$$

$$Q = \langle E_x^2 \rangle - \langle E_y^2 \rangle, \tag{2}$$

$$U = 2 \cdot \mathrm{Re}(E_x E_y^*), \tag{3}$$

$$V = -2 \cdot \mathrm{Im}\langle E_x E_y^* \rangle, \tag{4}$$

where the expression of the electric field in rectangular (Cartesian) coordinates is expressed as

$$\overline{E} = E_x \hat{x} + E_y \hat{y}. \tag{5}$$

The final application of the instrument is to measure the polarization of the CMB, which is considered a linearly polarized wave, and therefore, the parameter V is expected to be 0.[24]

The schematic of the microwave interferometer composed of two receivers is shown in Fig. 2. Each receiver comprises a front-end module (FEM) cooled down to 20 K and back-end module (BEM) at 300 K. The FEM is cooled to cryogenic temperature to reduce thermal noise as much as possible. In the FEM, both horns receive an incident radiation, which is separated into two components through a polarizer connected to an orthomode transducer (OMT), behaving both together as a broadband septum polarizer. The $(\hat{x}, \hat{y})$ axis orientation of the incident field is defined by the OMT, and the polarizer is rotated 45 deg along the x axis of the OMT. Those two output components of the OMT are proportional to the left (E_L) and right (E_R) circularly polarized components of the incident radiation expressed as

$$\overline{E} = E_L \hat{l} + E_R \hat{r}, \tag{6}$$

where $\hat{l} = \frac{\hat{x}+j\hat{y}}{\sqrt{2}}$ and $\hat{r} = \frac{\hat{x}-j\hat{y}}{\sqrt{2}}$ are the left and right unit vectors, respectively. Moreover, the rectangular components of the electric field expressed in terms of the left and right polar components of the electric field can be written as $E_x = \frac{E_L+E_R}{\sqrt{2}}$ and $E_y = j\frac{E_L-E_R}{\sqrt{2}}$.

Furthermore, the OMT outputs, through the waveguide to coaxial adapters, become voltages v_L and v_R, proportional to the left and right circularly polarized components E_L and E_R, respectively. Those voltages are amplified in ultra-low-noise amplifiers (LNAs) and cooled down to a physical temperature of 20 K in the FEM. Afterward, in the BEM, both voltages are further amplified, phase-shifted, filtered, divided into two frequency bands and then combined in a correlation module. A high speed phase switching technique is implemented in each BEM to reduce $1/f$ noise, providing eight outputs, four of them for the low frequency band and the other four for the high one.

Once the system is described, an analysis of the system noise temperature based on all noise contributions in a ground-based receiver is performed. Moreover, an analysis of the microwave receiver is included, in order to show the microwave receiver output expressions as a function of incident wave components and, therefore, of the Stokes parameters.

3.1 *Noise Analysis*

The interferometer is a ground-based instrument, so the operation noise temperature is the contribution of the atmosphere and the noise temperature of the receiver. The operation noise temperature, T_op, at the input of the cryostat window as reference plane is given by[25]

$$T_\mathrm{op} = \frac{T_\mathrm{CMB} + T_\mathrm{atm}}{L_\mathrm{atm}} + T_\mathrm{sys}, \tag{7}$$

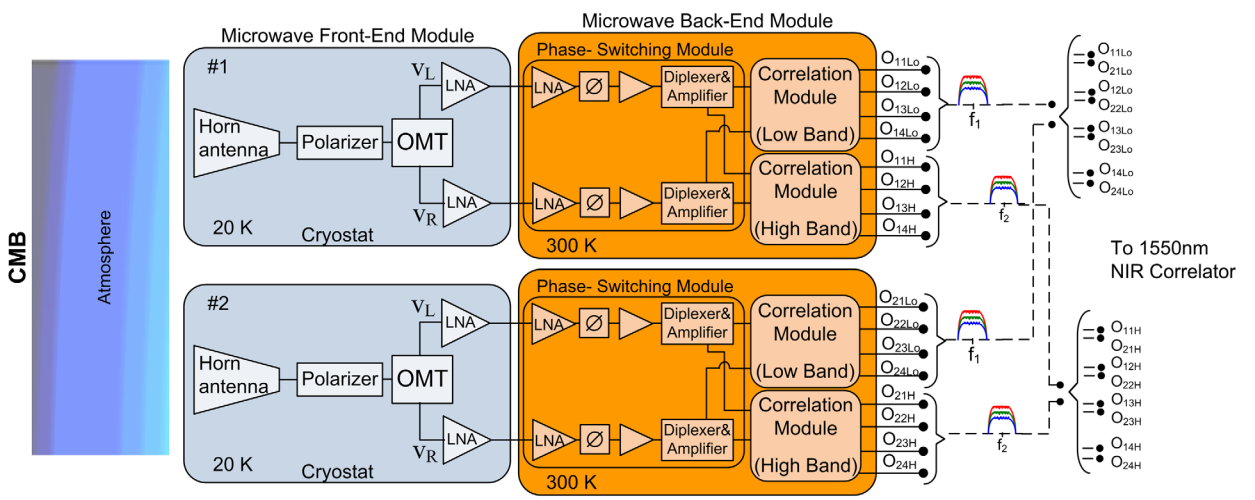

Fig. 2 Microwave interferometer composed of two receivers: the FEM operates at cryogenic temperature (in blue) and the BEM (in orange) works at room temperature.

where T_{CMB} is the brightness temperature of the CMB, T_{atm} is the effective atmospheric temperature, L_{atm} is the attenuation through the atmosphere, and T_{sys} is the effective noise temperature of the system. The contributions to the system noise temperature are the microwave receiver effective noise temperature, the fraction of noise power received from the ground ($T_{spillover}$) and all the other parts that make up the receiver. Among these contributing subsystems, the vacuum window of the cryostat, the infrared filter ($T_{IRfilter}$) in front of the horn antenna, and the whole microwave receiver are taken into account. Hence, FEM and BEM modules provide noise temperatures and gains (T_{window}, G_{window}), ($T_{IRfilter}$, $G_{IRfilter}$), (T_{FEM}, G_{FEM}) and (T_{BEM}, G_{BEM}), respectively. In case of installing the instrument in a telescope, the contribution to the noise temperature of the reflector increases the system noise temperature. The reflector noise temperature due to resistivity losses of mirror surface would be considered taking into account its dependence on the incident wave polarization.[25] Since the interferometer will operate without a telescope, the reflector noise contribution to the system is not considered. Therefore, the system noise temperature is given by

$$T_{sys} = T_{spillover} + T_{rec}. \tag{8}$$

The CMB temperature and effective atmospheric temperature are present in any ground receiver. On the other hand, spillover temperature and the microwave receiver noise temperature depend on all the instrument subsystems, mainly on the passive elements and the cryogenic LNAs in the FEM. The receiver noise temperature can be written as

$$T_{rec} = T_{window} + \frac{T_{IRfilter}}{G_{window}} + \frac{T_{FEM}}{G_{window}G_{IRfilter}} + \frac{T_{BEM}}{G_{window}G_{IRfilter}G_{FEM}}, \tag{9}$$

$$G_{FEM} = G_{HPO}G_{LNA\_FEM}, \tag{10}$$

$$T_{FEM} = (L_{HPO} - 1) \cdot T_{phys} + \frac{T_{LNA\_FEM}}{G_{HPO}}, \tag{11}$$

where L_{HPO} is the insertion loss of waveguide elements in the FEM, including contributions of the horn antenna, polarizer, and OMT, and G_{HPO} is $\frac{1}{L_{HPO}}$. T_{phys} is the cryogenic physical temperature, T_{LNA_FEM} and G_{LNA_FEM} are the equivalent noise temperature and gain of the cryogenic LNA in the FEM. The BEM noise temperature is given by

$$T_{BEM} = T_{LNA1\_BEM} + \frac{T_{PS}}{G_{LNA1\_BEM}} + \frac{T_{LNA2\_BEM}}{G_{LNA1\_BEM}G_{PS}} + \frac{T_D}{G_{LNA1\_BEM}G_{PS}G_{LNA2\_BEM}} + \frac{T_{LNA3\_BEM}}{G_{LNA1\_BEM}G_{PS}G_{LNA2\_BEM}G_D} + \frac{T_{corr}}{G_{LNA1\_BEM}G_{PS}G_{LNA2\_BEM}G_DG_{LNA3\_BEM}}, \tag{12}$$

where T_{LNAi_BEM} and G_{LNAi_BEM} are the equivalent noise temperatures and gains of each LNA in the BEM ($i = 1, 2, 3$). T_{PS}, G_{PS}, T_D, G_D, and T_{corr} are the equivalent noise temperatures and gains of the phase shifter, diplexer, and correlation module.

The BEM equivalent noise temperature can be simplified to T_{LNA1_BEM} since the gain of the FEM together with the gain G_{LNA1_BEM} is high enough to neglect the contributions of the following subsystems to the receiver noise temperature. Therefore, the receiver noise temperature can be simplified as

$$T_{rec} = T_{window} + \frac{T_{IRfilter}}{G_{window}} + \frac{(L_{HPO} - 1) \cdot T_{phys}}{G_{window}G_{IRfilter}} + \frac{T_{LNA\_FEM}}{G_{window}G_{IRfilter}G_{HPO}} + \frac{T_{LNA1\_BEM}}{G_{window}G_{IRfilter}G_{HPO}G_{FEM}}. \tag{13}$$

The contributions to the operation noise temperature from 10 to 20 GHz of the CMB and the atmosphere are listed in Table 1. The atmospheric attenuation is calculated from water vapor data measured at Izaña Observatory above 2400 m (Tenerife, Spain) with the Cernicharo 1989 ATM code,[26] as reference site for a ground-based instrument.

Table 1 Contributions to the operation temperature from 10 to 20 GHz at Izaña Observatory above 2400 m (Tenerife, Spain).

Description	Noise temperature (K)	Attenuation
CMB	$T_{CMB} = 2.725$	
Atmosphere	$T_{atm} = 2.37$	$L_{atm} = 1.00935$

3.2 *Receiver Analysis*

The analysis of the microwave receiver consists of obtaining the signal output expressions of the receiver for an incident polarized wave. For the presented prototype, the microwave receiver is analyzed from the cryogenic LNAs in the FEM to the outputs in the BEM, as shown in a simplified schematic in Fig. 3. Input voltages v_L and v_R are proportional to the left and right circularly polarized components coming from the OMT into the FEM, which go through separated branches called branch#1 and branch#2. The first element in each branch is a LNA followed by a phase switch that allows the phase to be switched between 0 deg and 360 deg with 5.625 deg step in each branch independently. After that, a diplexer splits the frequency band in two subbands: 10 to 14 GHz and 16 to 20 GHz. Then, each sub-band voltage at the diplexers outputs is amplified and introduced into the correlation module. In each correlation module, the two input voltages are split in two after being combined with 90 deg hybrid couplers. The correlation module provides a combination of the two input components, v_L and v_R, split into four outputs.

Output signals for each subsystem in the microwave receiver, Fig. 3, can be determined. Considering the input voltages into the microwave receiver proportional to the left and right circularly polarized components of the incident electromagnetic field, v_L and v_R, respectively, all output signals from the subsystems are summarized in Tables 2 and 3.

g_i represents the voltage gains of front-end cryogenic amplifiers and back-end amplifiers. A_i represents the voltage loss of the passive elements in the BEM. Magnitudes n_i and φ_i represent noise voltages and signal phases of front-end cryogenic amplifiers and back-end amplifiers and passive elements. Finally, ϕ_i represents the phase shift in the different switch states.

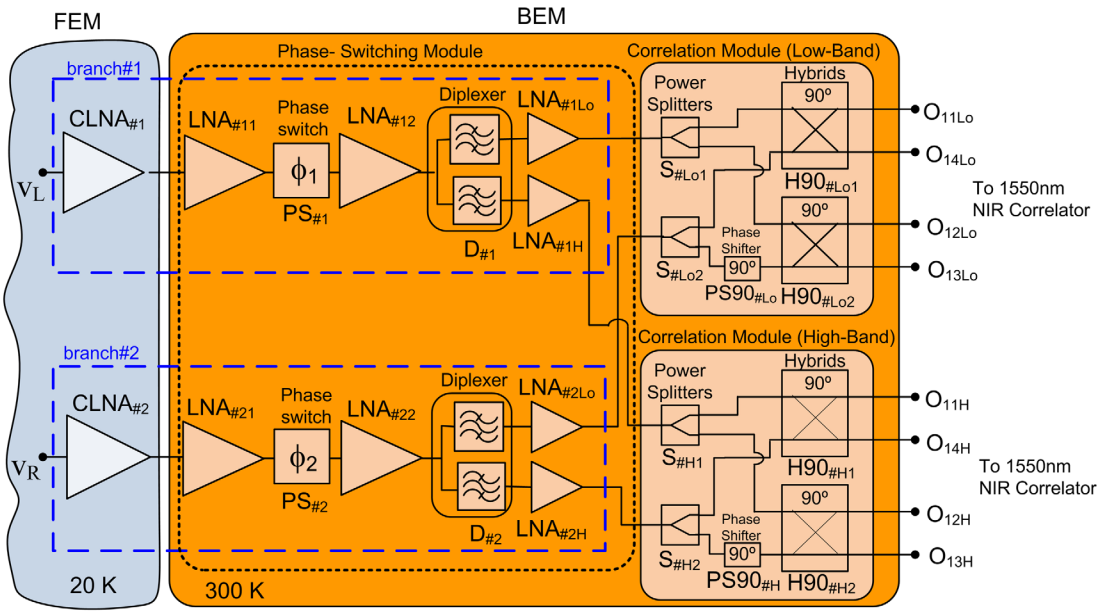

Fig. 3 Schematic of circuitry part in the microwave receiver.

Table 2 Microwave receiver output signals from each subsystem: branch#1 ($k = 1$) and branch#2 ($k = 2$).

Subsystem	Output signal
Cryogenic amplifier: CLNA#k	$v_{okca} = g_{cak}(v_{\text{in}} + n_{cak})e^{-j\varphi_{cak}}$ $v_{\text{in}} = v_L(k = 1);\ v_{\text{in}} = v_R(k = 2)$
Low-noise amplifier: LNA#k1	$v_{oka1} = g_{ak1}(v_{okca} + n_{ak1})e^{-j\varphi_{ak1}}$
Phase-switch: PS#k $\phi_k = 0$ deg, 5.625 deg, 11.25 deg, ... 360 deg	$v_{okps} = A_{psk}(v_{oka1} + n_{psk})e^{-j\phi_k}$
Low-noise amplifier: LNA#k2	$v_{oka2} = g_{ak2}(v_{okps} + n_{ak2})e^{-j\varphi_{ak2}}$
Diplexer: D#k	$v_{okdLo} = A_{dkLo}(v_{oka2} + n_{dkLo})e^{-j\varphi_{dkLo}}$ $v_{okdH} = A_{dkH}(v_{oka2} + n_{dkH})e^{-j\varphi_{dkH}}$
Amplifier: LNA#kLo	$v_{okaLo} = g_{akLo}(v_{okdLo} + n_{akLo})e^{-j\varphi_{akLo}}$
Amplifier: LNA#kH	$v_{okaH} = g_{akH}(v_{okdH} + n_{akH})e^{-j\varphi_{akH}}$

Table 3 Correlation Module subsystems output signals: low-band (B = Lo) and high-band (B = H).

Subsystem	Output signal
Power splitters: S#B1	$v_{oisB1} = \frac{1}{\sqrt{2}}A_{sB1}(v_{o1aB} + n_{sB1})e^{-j\varphi_{sB1}}\ \ i = 1,2$
Power splitter: S#B2	$v_{oisB2} = \frac{1}{\sqrt{2}}A_{sB2}(v_{o2aB} + n_{sB2})e^{-j\varphi_{sB2}}\ \ i = 1,2$
90 deg phase-shifter: PS90#B	$v_{ops90B} = A_{ps90B}(v_{o2sB2} + n_{ps90B})e^{-j\frac{\pi}{2}}$
Hybrid 90 deg: H90#B1	$v_{O11B} = \frac{1}{\sqrt{2}}A_{h90B1}(v_{o1sB1}e^{-j\frac{\pi}{2}} - v_{o1sB2})$ $v_{o14B} = \frac{1}{\sqrt{2}}A_{h90B1}(-v_{o1\ sB1} + v_{o1sB2}e^{-j\frac{\pi}{2}})$
Hybrid 90 deg: H90#B2	$v_{o12B} = \frac{1}{\sqrt{2}}A_{h90B2}(v_{o2sB1}e^{-j\frac{\pi}{2}} - v_{ops90B})$ $v_{o13B} = \frac{1}{\sqrt{2}}A_{h90B2}(-v_{o2sB1} + v_{ops90B}e^{-j\frac{\pi}{2}})$

The output voltages of the microwave receiver are proportional to a combination of the left and right circularly polarized components of the incident wave, together with the receiver noise. The significant noise voltages to the receiver noise are only n_{cak} and n_{ak1}, which belong to the cryogenic LNA and the first LNA in the BEM, respectively. Those noise voltages are amplified and the contributions to the noise of the following subsystems are considered negligible. The output voltages from each branch (#1 and #2) in Fig. 3 are v_{okaLo} and v_{okaH}, which are the inputs to the low-band correlator and high-band correlator respectively, expressed as

$$v_{okaLo} = G_{Tk} \cdot G_{TkLo} \cdot [n_{ak1} + g_{cak} \cdot (n_{cak} + v_{\text{in}}) \cdot e^{-j\varphi_{cak}}] \cdot e^{-j(\phi_{Tk}+\varphi_{kLo})}, \tag{14}$$

$$v_{okaH} = G_{Tk} \cdot G_{TkH} \cdot [n_{ak1} + g_{cak} \cdot (n_{cak} + v_{\text{in}}) \cdot e^{-j\varphi_{cak}}] \cdot e^{-j(\phi_{Tk}+\varphi_{kH})}, \tag{15}$$

with $k = 1$, $v_{\text{in}} = v_{\text{L}}$ (left) for branch#1 and $k = 2$, $v_{\text{in}} = v_{\text{R}}$ (right) for branch#2. Magnitudes ϕ_{kT} and G_{kT} represent the phase and gain of the group composed of first and second LNA and phase switch in the BEM, whereas φ_{kLo}, φ_{kH}, G_{kTLo}, and G_{kTH} are the phases and gains of the diplexer together with the following LNA in each frequency band (Lo = low-band; H = high-band) in the BEM. These phases and gains are expressed as

$$\phi_{Tk} = \varphi_{ak1} + \phi_k + \varphi_{ak2}, \tag{16}$$

$$\phi_{TkB} = \varphi_{dkB} + \varphi_{akB} \quad (B = \text{Lo}, \text{H}), \tag{17}$$

$$G_{Tk} = g_{ak1} \cdot A_{PSk} \cdot g_{ak2}, \tag{18}$$

$$G_{TkB} = A_{dkB} \cdot g_{akB} \quad (B = \text{Lo}, \text{H}), \tag{19}$$

where v_{o11B}, v_{o14B}, v_{o12B}, and v_{o13B} are the four outputs voltages of each correlator, with B indicating the low-band correlator (B = Lo) or the high-band correlator (B = H), which are given by

$$v_{O1mB} = \frac{A_{h90B1}}{2}(-j^m \cdot G_1 \cdot v_1 \cdot e^{-j\Theta_1} + (-1)^m \cdot j^{m-1} \cdot G_2 \cdot v_2 \cdot e^{-j\Theta_2}); \quad m = 1,4, \tag{20}$$

$$v_{O1nB} = \frac{A_{h90B2}}{2}((-j)^{n-1} \cdot G_1 \cdot v_1 \cdot e^{-j\Theta_1} + j^{n-1} \cdot G_2 \cdot (A_{ps90B})^{n-2} \cdot v_2 \cdot e^{-j\Theta_2}); \quad n = 2,3, \tag{21}$$

where the phases Θ_1, Θ_2, the gains G_1, G_2, and the voltages v_1, v_2 are expressed as

$$\Theta_1 = \phi_{T1} + \phi_{T1B} + \varphi_{sB1}, \tag{22}$$

$$\Theta_2 = \phi_{T2} + \phi_{T2B} + \varphi_{sB2}, \tag{23}$$

$$G_1 = G_{T1} \cdot G_{T1B} \cdot A_{sB1}, \tag{24}$$

$$G_2 = G_{T2} \cdot G_{T2B} \cdot A_{sB2}, \tag{25}$$

$$v_1 = n_{a11} + g_{ca1} \cdot (n_{ca1} + v_L) \cdot e^{-j\varphi_{ca1}}, \tag{26}$$

$$v_2 = n_{a21} + g_{ca2} \cdot (n_{ca2} + v_R) \cdot e^{-j\varphi_{ca2}}. \tag{27}$$

In order to show the relationship of the output voltages with the Stokes parameters, some considerations are fulfilled. Each pair of subsystems in branch#1 and branch#2 is considered to be identical in terms of gains and loss voltages ($G_{T1} = G_{T2}$, $G_{T1B} = G_{T2B}$) as well as in terms of phase, except for the phase switches, $\phi_1 \neq \phi_2$. Besides, both power splitters as well as both 90 deg hybrids in the correlation module have the same loss voltages ($A_{sB1} = A_{sB2}$, $A_{h90B1} = A_{h90B2}$). Moreover, the voltage gain of the 90 deg phase shifter in the correlation modules is $A_{ps90B} = 1$. Then, the four outputs of each correlator, with B = Lo for the low-band correlator and B = H for the high band correlator, are given by

$$v_{O1mB} = \frac{G_{TB}}{2}(-j^m \cdot v_1 + (-1)^m \cdot j^{m-1} \cdot v_2 \cdot e^{-j\phi_B}) \cdot e^{-j\phi_{TB}}; \quad m = 1,4, \tag{28}$$

$$v_{O1nB} = \frac{G_{TB}}{2}((-j)^{n-1} \cdot v_1 + j^{n-1} \cdot v_2 \cdot e^{-j\phi_B}) \cdot e^{-j\phi_{TB}}; \quad n = 2,3, \tag{29}$$

where ϕ_{TB}, ϕ_B and G_{TB} represent the phases and voltage gains of all the elements in each branch including the voltage loss of the elements in the correlation module, which are expressed as

$$\phi_{1B} = \varphi_{a11} + \phi_1 + \varphi_{a12} + \varphi_{d1B} + \varphi_{a1B} + \varphi_{sB1}, \tag{30}$$

$$\phi_B = \phi_2 - \phi_1, \tag{31}$$

$$G_{TB} = g_{a11} \cdot A_{PS1} \cdot g_{a12} \cdot A_{d1B} \cdot g_{a1B} \cdot A_{sB1} \cdot A_{h90B1}. \tag{32}$$

In the case of a noiseless receiver ($n_{cak} = 0$, $n_{ak1} = 0$), the output voltages are directly related to the left and right circularly polarized components of the incident wave as

$$v_{O1mB} = \frac{G_B}{2}(-j^m \cdot v_L + (-1)^m \cdot j^{m-1} \cdot v_R \cdot e^{-j\phi_B}) \cdot e^{-j\phi_{TB}}; \quad m = 1,4, \tag{33}$$

$$v_{O1nB} = \frac{G_B}{2}((-j)^{n-1} \cdot v_L + j^{n-1} \cdot v_R \cdot e^{-j\phi_B}) \cdot e^{-j\phi_{TB}}; \quad n = 2,3, \tag{34}$$

where $G_B = g_{ca1} \cdot G_{TB}$.

The power at the four outputs of each correlator for a load impedance $Z_L = 1$ Ohm ($\lfloor v_{OB} \rfloor^2$) in terms of the Stokes parameters, with $v_L = |v_L|e^{j\phi_L}$ and $v_R = |v_R|e^{j\phi_R}$, can be written as

$$P_{O1mB} = \frac{|G_B|^2}{4}(I + (-1)^m \cdot U \cdot \cos\phi_B + (-1)^m \cdot Q \cdot \sin\phi_B); \quad m = 1,4, \tag{35}$$

$$P_{O1nB} = \frac{|G_B|^2}{4}(I + (-1)^{n-1} \cdot Q \cdot \cos\phi_B + (-1)^n \cdot U \cdot \sin\phi_B); \quad n = 2,3, \tag{36}$$

with the Stokes parameters expressed as $I = |v_L|^2 + |v_R|^2$, $Q = +2\,\mathrm{Re}(v_L^* v_R)$, $U = -2\,\mathrm{Im}(v_L^* v_R)$, and $V = |v_L|^2 - |v_R|^2$.

The outputs powers with four different phase-switches states are summarized in Table 4.

4 Microwave Receiver Design

In this section, all the microwave subsystem designs and their measurement performance in both FEM and BEM are described. The microwave receiver scheme, depicted in Fig. 2, is based on subsystems covering the full frequency range from 10 to 19.5 GHz, apart from the correlation modules specially designed for the sub-bands: 10 to 14 GHz and 16 to 20 GHz.

4.1 *Front-End Module*

4.1.1 *Horn antenna*

The horn antenna is designed to cover the whole 10 to 19.5 GHz bandwidth, optimizing its efficiency, gain, low cross-polarization, and low side lobes. The more difficult requirements of the horn antenna are the bandwidth and the cross-polar response, which affect the sensitivity to polarization, therefore, a circular horn has been specifically designed. Horn longitudinal profile is based on an optimized spline curve to achieve a good trade-off between bandwidth, cross-polarization, impedance matching, and directivity. The horn antenna is designed for at least 20 dB

Table 4 Output powers for phase differences between branches of 0 deg, 90 deg, 180 deg, and 270 deg.

ϕ_B (deg)	P_{O11B}	P_{O14B}	P_{O12B}	P_{O13B}
0	$\frac{\lvert G_{TB}\rvert^2}{4}(I-U)$	$\frac{\lvert G_{TB}\rvert^2}{4}(I+U)$	$\frac{\lvert G_{TB}\rvert^2}{4}(I-Q)$	$\frac{\lvert G_{TB}\rvert^2}{4}(I+Q)$
90	$\frac{\lvert G_{TB}\rvert^2}{4}(I-Q)$	$\frac{\lvert G_{TB}\rvert^2}{4}(I+Q)$	$\frac{\lvert G_{TB}\rvert^2}{4}(I+U)$	$\frac{\lvert G_{TB}\rvert^2}{4}(I-U)$
180	$\frac{\lvert G_{TB}\rvert^2}{4}(I+U)$	$\frac{\lvert G_{TB}\rvert^2}{4}(I-U)$	$\frac{\lvert G_{TB}\rvert^2}{4}(I+Q)$	$\frac{\lvert G_{TB}\rvert^2}{4}(I-Q)$
270	$\frac{\lvert G_{TB}\rvert^2}{4}(I+Q)$	$\frac{\lvert G_{TB}\rvert^2}{4}(I-Q)$	$\frac{\lvert G_{TB}\rvert^2}{4}(I-U)$	$\frac{\lvert G_{TB}\rvert^2}{4}(I+U)$

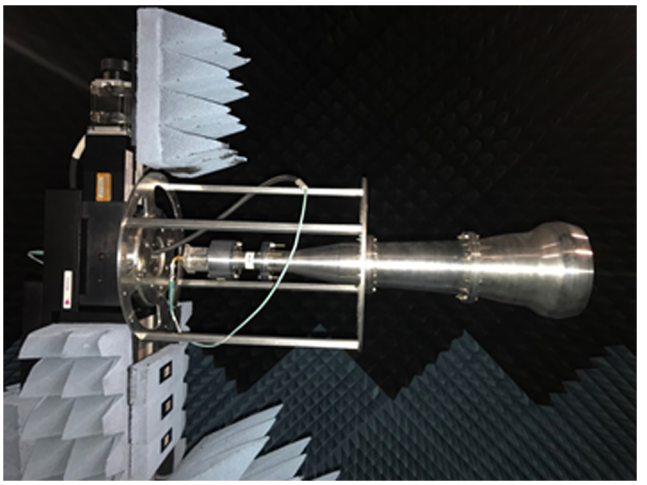

Fig. 4 Horn antenna assembled in the anechoic chamber.

gain, which involves an aperture size of 128 mm. On the other hand, the circular waveguide with a diameter 9.41 mm is chosen as an input port. The diameter is optimum for impedance matching over the whole frequency band as well as for connection to the polarizer. The horn antenna supported by a customized structure for testing in the anechoic chamber is shown in Fig. 4. The horn antenna is machined from aluminum and consists of three sections.

The return loss measured at the circular waveguide port of the antenna is shown in Fig. 5. The test was done including two special designed adapters, one circular waveguide to rectangular waveguide with several octagonal-shaped sections, and another one from a rectangular waveguide to coaxial.[27,28] The return loss is better than 20 dB from 10 to 19.5 GHz. Insertion loss was measured placing an effective short in front of the horn with a flat copper plate, obtaining an average value of −0.075 dB over the band. Horn transmission efficiency at room temperature is 98%, which is expected to increase slightly when cooled down to 20 K considering the reduction of resistive losses.[29]

The radiation patterns of the horn antenna at 13 and 18 GHz are shown in Fig. 6. The figures show the copolar and the cross-polar patterns. These tests show a typical level of cross-polarization lower than −25 dB from 10 to 19.5 GHz.

4.1.2 *Polarizer*

The designed polarizer is a square quad-ridge waveguide device with broadband performance and low axial ratio. This polarizer is a differential 90 deg phase shifter for the two orthogonal propagation modes (TE_{10} and TE_{01}) in the square waveguide. The constant phase difference between the two modes is obtained using internal stepped ridges in the four walls of the square waveguide. The design is based on Ref. 30. When the electric field at the polarizer input has a linear orientation, each orthogonal component, in the 45 deg rotated axis of the polarizer, propagates along the ridged square waveguide with different insertion phase and, therefore, at the polarizer output, the components have a 90 deg phase difference between them.

A view of the fabricated polarizer machined from aluminum is shown in Fig. 7. The length of the polarizer is 136.87 mm and the square waveguide dimension is $a = b = 16.8$ mm. The polarizer is connected to the output circular waveguide of the horn through a circular to square waveguide adapter.

Figure 8(a) shows measurement results of the polarizer for insertion and return loss, and Fig. 8(b) shows the phase and amplitude difference between the transmission modes TE_{10} and TE_{01}. Insertion loss is around 0.15 dB and return loss better than 20 dB for both transmission modes over the frequency band. The measured amplitude difference is 0.02 dB and the phase difference from 10.1 to 19.65 GHz is $90° \pm 4°$. This phase difference corresponds to an axial ratio of 0.4 dB, which together with the horn-antenna cross-polarization plays an important role in the polarization sensitivity of the instrument.

4.1.3 *Orthomode transducer*

The designed OMT covers almost an octave bandwidth from 10 to 19.46 GHz. It is a turnstile-junction-based OMT, which has been assembled in a platelet configuration with three layers.[31] The input port of the OMT is a circular waveguide with a diameter of 9.41 mm and the two rectangular waveguides at the output are rectangular waveguides with $a = 15.4$ mm and $b = 7.7$ mm. The OMT machined in aluminum is shown in Fig. 9. The external size of the OMT is 132.5×132.5 mm^2 and the three layers' thickness is 29.85 mm.

Measurement results of return loss, insertion loss, isolation as well as amplitude and phase imbalances, between the

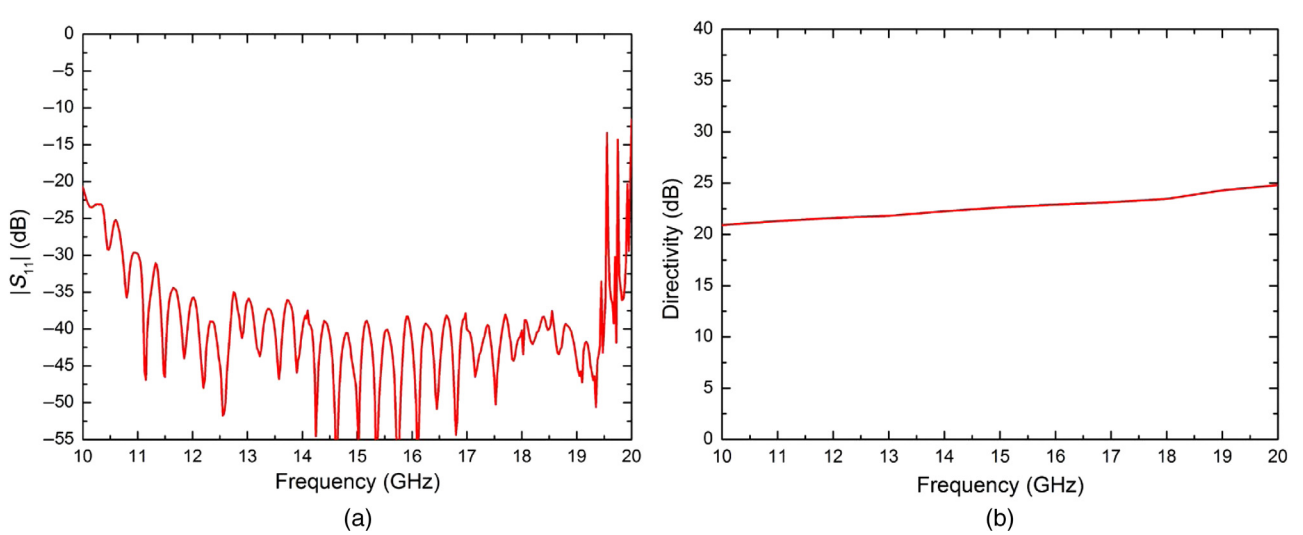

Fig. 5 Horn antenna measurement results: (a) return loss (|S11|) and (b) directivity.

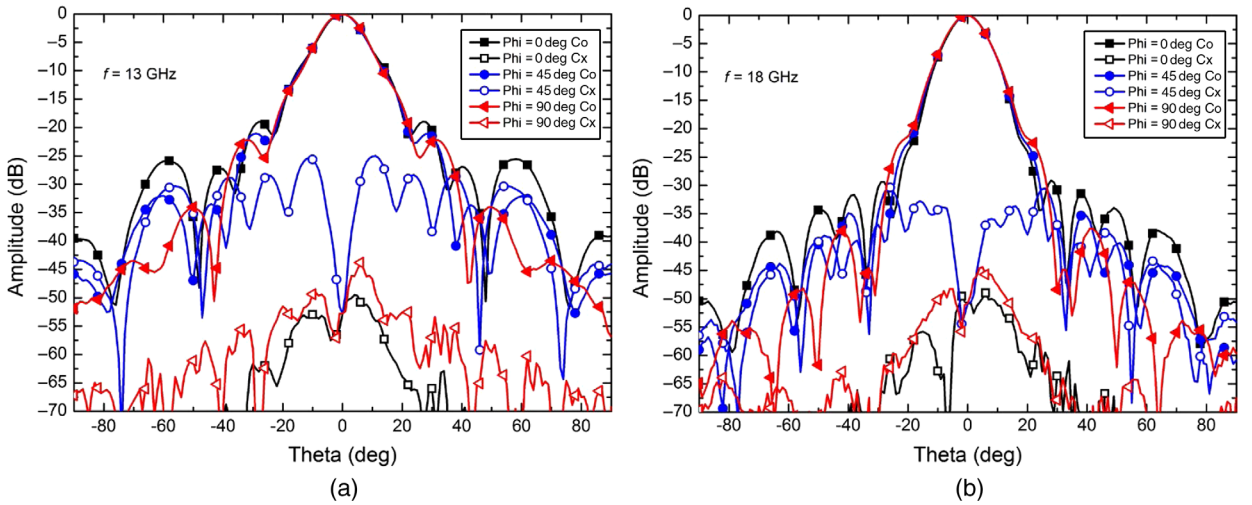

Fig. 6 Amplitude radiation pattern measurements of the horn antenna. Results at 13 GHz and 18 GHz of the copolar (Co) and cross-polar (Cx) responses.

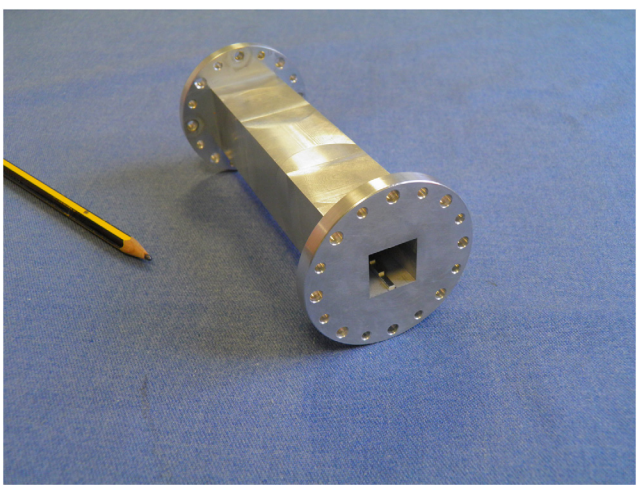

Fig. 7 Polarizer. View of the squared waveguide. Internal dimension $a = b = 16.8$ mm.

transmissions from the circular waveguide to each rectangular output of the OMT, are shown in Fig. 10. The insertion loss is better than 0.2 dB and the return loss higher than 25 dB with isolation between the rectangular ports is better than 45 dB. The cutoff frequency of the structure is 9.73 GHz, therefore, the insertion loss increases at lower frequencies, and the maximum operating frequency without higher order modes is 19.46 GHz. Moreover, the phase and amplitude differences between the transmissions from the circular waveguide to each rectangular output are $0° \pm 1.5°$ and ± 0.015 dB, respectively, with a higher difference at the lower edge of the frequency band.

4.1.4 *Polarizer + OMT*

In the FEM, the combination together of polarizer and OMT performs like a septum polarizer, with a 45 deg rotation of the polarizer along the x axis of the OMT. The advantage of the adopted solution is the wider bandwidth obtained compared to a septum polarizer, which typically has 15% to 20% of bandwidth.[32,33]

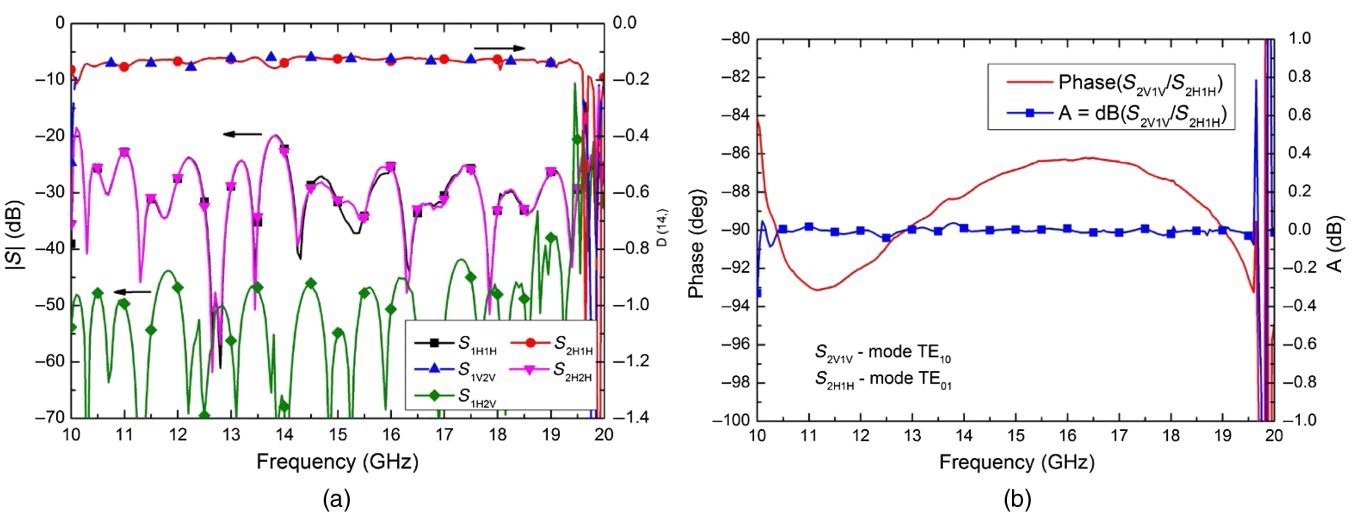

Fig. 8 Polarizer measurements. The input square waveguide physical port is #1 with electrical ports #1V and #1H, and the output squared waveguide physical port is #2 with electrical port #1V and #1H. V indicates the transmission mode TE10 and H indicates the transmission mode TE01. (a) Insertion loss and return loss of the mode TE10. (b) Phase and amplitude difference between transmission modes TE10 and TE01 in the square waveguide.

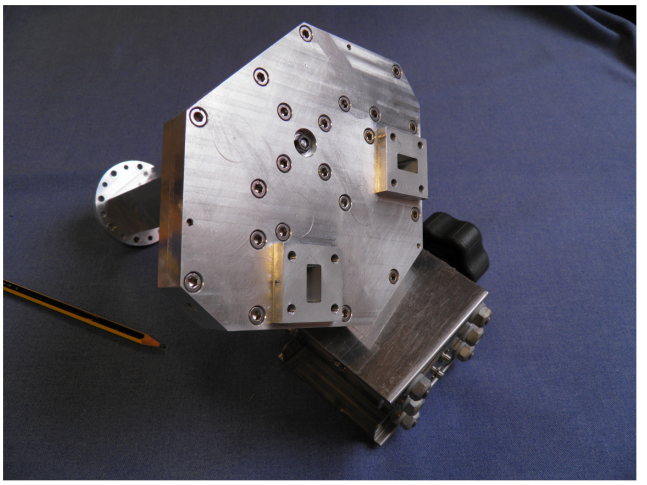

Fig. 9 OMT. Rectangular waveguide outputs side.

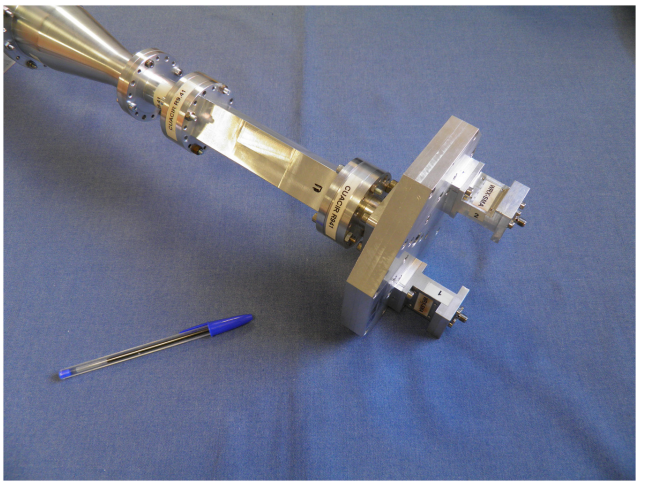

Fig. 11 Polarizer and OMT assembly. The polarizer is connected between the horn antenna and the OMT. Coaxial to rectangular waveguide adapters are connected to each OMT rectangular waveguide output.

Figure 11 shows the assembly of the polarizer connected between the horn antenna and the OMT. This combination polarizer-OMT has three physical ports and four electrical ports, because, at the polarizer input, there are two orthogonal modes. On the condition that the incident field is defined by the OMT $(\hat{x}, \hat{y})$ axis orientation, with an input horizontal electric field E along the x axis, coming into the 45 deg rotated polarizer rectangular waveguide port, the two OMT output signals have the same amplitude but are phase shifted 90 deg. Consequently, the outputs from the OMT are the left and right polar components of the incident field. On the other hand, if a signal is introduced only in one rectangular waveguide port of the OMT, then at the polarizer output, a circularly polarized wave is obtained, right or left hand polarized according to the selected input port.

4.1.5 *Cryogenic low noise amplifiers*

The amplifiers in the FEM are broadband hybrid LNAs working at cryogenic temperature. They are based on discrete 50-nm gate length methamorphic high-electron mobility technology transistors from Fraunhofer IAF.[34,35] They are three-stage amplifiers covering the whole frequency band. A photograph of the amplifier without cover is depicted in Fig. 12(a). Test results of gain and noise temperature of a typical amplifier unit are shown in Fig. 12(b) when it is cooled down to 20 K. The average noise temperature is 13.5 K and its average gain is 23.9 dB from 10 to 20 GHz. The power consumption is 6.43 mW.

4.2 *Back-End Module*

4.2.1 *Room temperature amplifiers*

Although the cryogenic amplifier defines the noise temperature of the instrument, LNAs are also used in the first stage of the BEM, working at room temperature. Commercial amplifiers

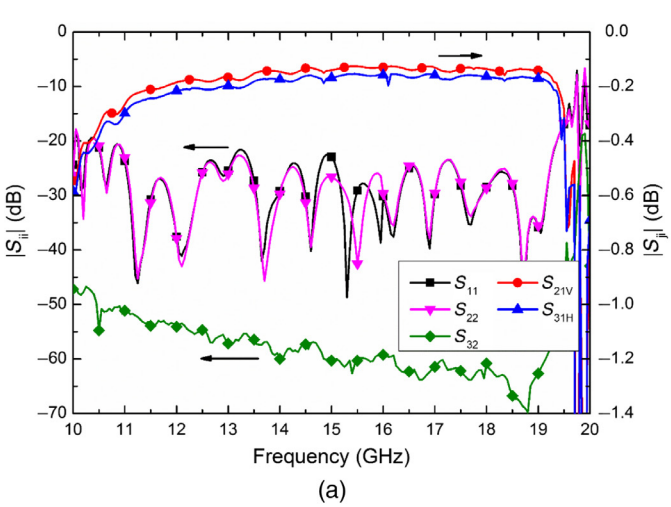

(a)

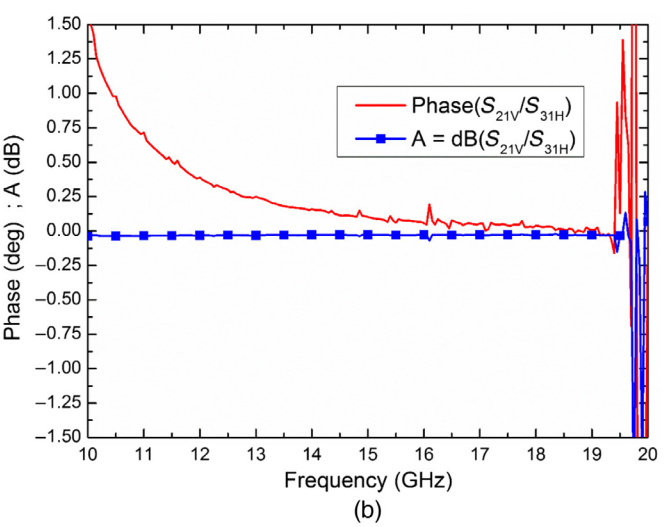

(b)

Fig. 10 OMT measurements. The circular waveguide physical port is #1 with two electrical ports #1V and #1H for the mode TE11. The rectangular waveguide ports are #2 and #3. (a) Insertion loss between the circular input waveguide port and the rectangular output waveguide ports (S21V, S31H), return loss of the circular waveguide port (S11), return loss of the rectangular waveguide port (S22), and isolation between rectangular ports (S32). (b) Amplitude and phase imbalances between transmissions from the circular waveguide to each rectangular waveguide output.

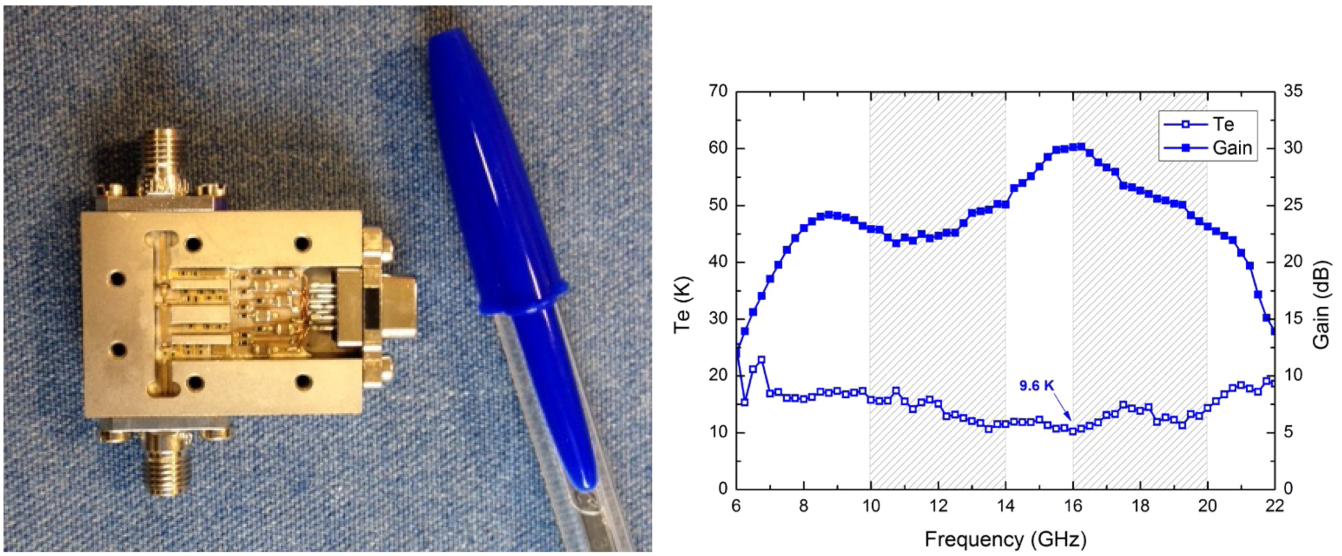

Fig. 12 Cryogenic LNA: (a) photograph of the amplifier and (b) gain and noise temperature measurements at 20 K.

from Analog Devices, model HMC565, with typical gain values of 20 and 2.6 dB of noise figure are used. This LNA is housed in an aluminum chassis with superSMA connectors from Southwest Microwave and its performance, in terms of gain and noise at ambient temperature, is shown in Fig. 13 (LNA 1—blue traces). On the other hand, in order to amplify the output signal from the diplexer, medium power amplifiers are used. These amplifiers are TGA2526 model from Qorvo, which have a broadband distributed topology with a typical gain of 17 dB and minimum output power for 1-dB gain compression point around +17 dBm. This amplifier is characterized in a chassis with coaxial connectors and its measurement results are shown in Fig. 13 (TGA1 red traces).

4.2.2 *Phase switch*

The phase switch is a Gallium Arsenide monolithic microwave integrated circuit 6-bit phase shifter, model CGY2173UH/C2 from OMMIC. Although the nominal frequency range is from 6 to 18 GHz, it can be extended up to 19.5 GHz. The CGY2173UH/C2 has a nominal phase-shifting range of 0 to 360° in 5.625° steps and uses an optimum combination of switched line and high pass/low pass filters, to obtain very low phase error and insertion loss variations. Figure 14 shows the insertion loss and phase-shifting measurement results for several phase states in the 10- to 20-GHz frequency band.

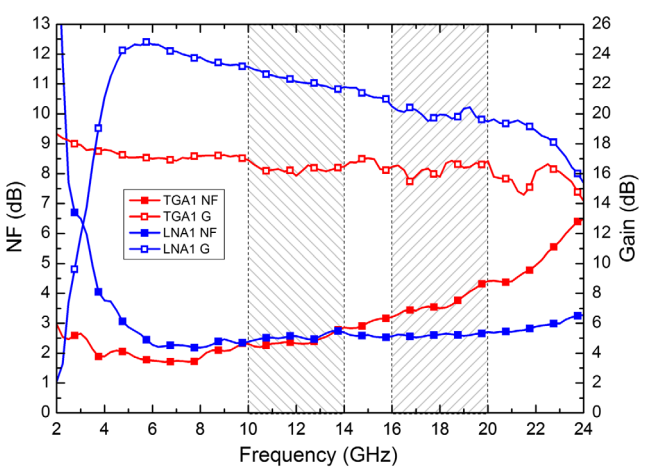

Fig. 13 Gain and noise figure measurements for the amplifiers HMC565 (LNA1 in blue) and TGA2526 (TGA1 in red) at 300 K.

4.2.3 *Diplexer*

The diplexer is a key part of the wideband very sensitive receiver since it needs to split the whole frequency band into two sub-bands: 10 to 14 GHz and 16 to 20 GHz to subsequent signal correlation in each sub-band of the receiver and to reject the 14 to 16 GHz band in between. The concept of the diplexer is based on a balanced configuration using hybrid couplers in the main circuit branch and high selective bandpass filters to confine both output bands based on Ref. 36. The combination of two 90 deg hybrid couplers with two identical bandpass filters of one band, which are placed in between, is used to extract the upper-frequency band. Then, a bandpass filter, designed in the other frequency band, confines the desired output band at the isolated port of the input coupler. Thus, the configuration for the diplexer shows that the upper-frequency band is connected through the hybrid couplers, whereas the lower band is obtained in the isolated port of the input hybrid. The diplexer, manufactured on a 0.254-mm-thick CLTE-XT substrate from Rogers Corporation, allocated in a chassis with superSMA connectors, is shown in Fig. 15(a). The measured transmission coefficients of both outputs are shown in Fig. 15(b). Insertion loss level of 3.3 dB and a rejection level between output bands higher than 20 dB have been achieved. A redesign of the diplexer would need to improve the achieved rejection in the 14 to 16 GHz in order to avoid interferences, as well as to limit the upper-frequency band to 16 to 19.5 GHz based on the achieved performance of other system components.

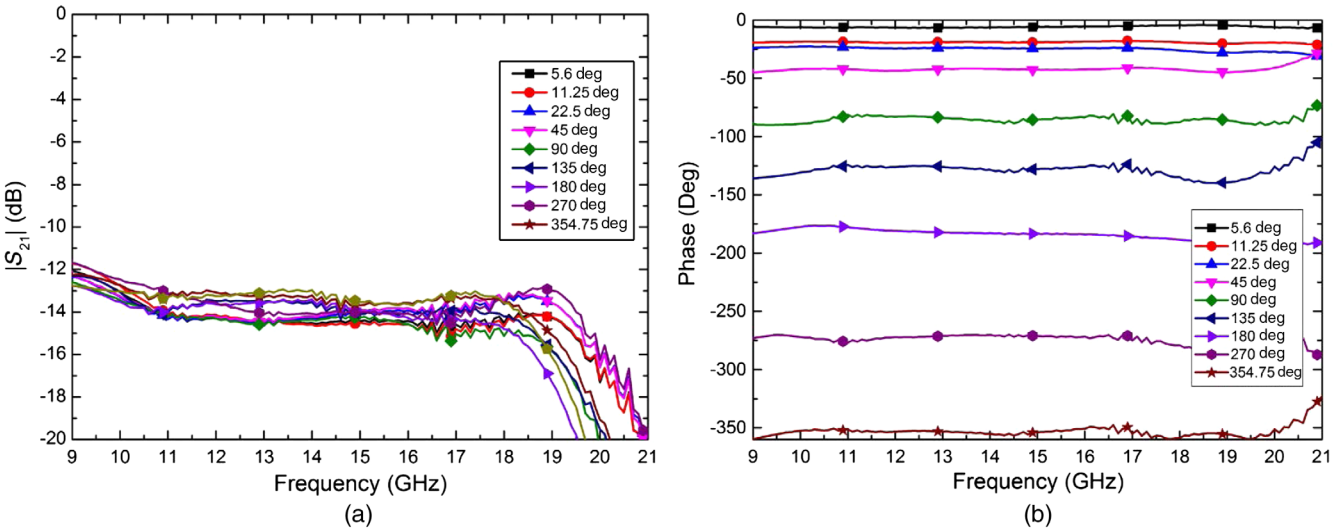

Fig. 14 Phase switch measurement results for several phase states: (a) insertion loss and (b) phase difference.

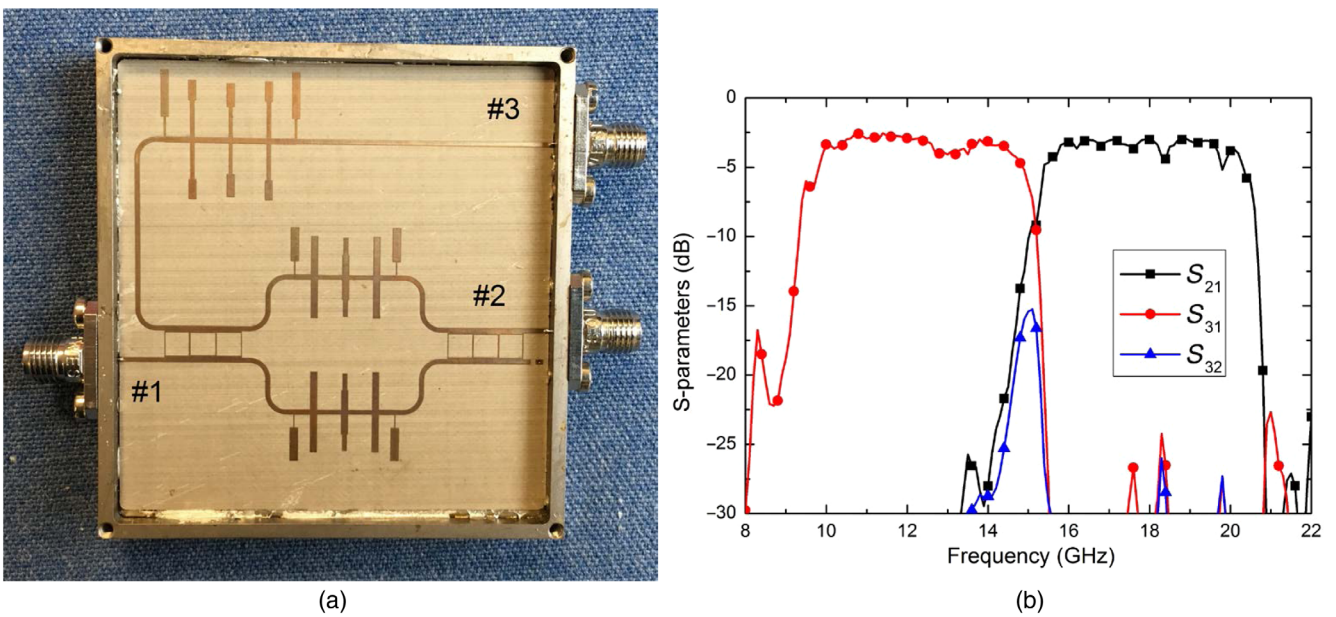

Fig. 15 (a) Photograph of the diplexer and (b) measured performance of the diplexer.

4.2.4 *Amplifiers and phase switch module*

Regarding the BEM, all the amplification stages, prior to the filtering section, as well as the phase switch, are integrated into a single module, in order to reduce interconnections and mismatching. Three HMC565 amplifiers and the CGY2173UH phase switch are housed in an aluminum chassis with superSMA connectors. A photograph of the module is depicted in Fig. 16.

4.2.5 *Microwave correlation module*

In this module, the two orthogonal components of the incoming signal, for each sub-band, are correlated. It is a six-port circuit with two input ports, one for each component, and four outputs, which are a linear combination of the Stokes parameters: I + Q, I − Q, I + U and I − U. For this purpose, Wilkinson power dividers, 90 deg hybrids and a 90 deg phase shifter are included, with a different design for each sub-band. The low frequency band correlation module, manufactured on 0.254-mm-thick CLTE-XT substrate from Rogers Corporation, allocated in a chassis with superSMA connectors, is shown in Fig. 17(a). Measurement results for this lower frequency band are depicted in Fig. 17(b). Insertion loss of 8 dB with isolation better than 20 dB is achieved in both frequency bands. The amplitude and phase differences between outputs are also shown in Fig. 18. Similar results have been obtained in the higher frequency band.

4.2.6 *BEM integration*

The integration of the BEM, working at ambient temperature, is made on an FR4 printed circuit board to allocate the microwave circuits as well as the DC circuit power supply. Figure 19(a) shows a photograph of a board with the assembly of a complete BEM composed of two branches and the two frequency band

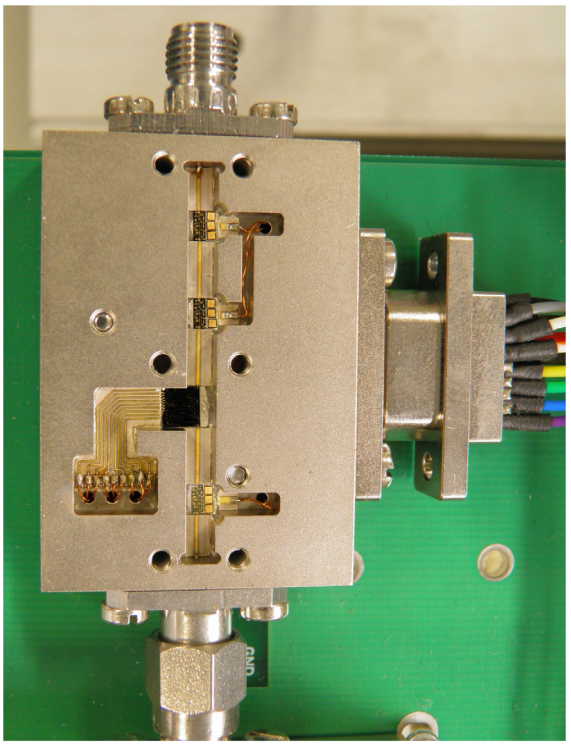

Fig. 16 Amplifiers and phase switch module in the BEM.

correlators in the center of the board. The two inputs to the BEM are in the foreground, and in the background, the eight connectors with four outputs per each frequency band of the BEM can be seen. Figure 19(b) shows four BEMs integrated into a 19 in standard rack.

5 System Characterization

This section is dedicated to the characterization of the microwave receiver. On one hand, some measurements are performed regarding only the BEM since the FEM is not relevant for the purpose of these measurements. On the other hand, the complete microwave receiver is taken into account for noise temperature results.

The integration of the microwave receiver with the electro-optical correlator working as the interferometer is out of the scope of this paper and it is described in Ref. 20, which shows synthesized images characterizing the polarization of an incoming signal through the Stokes parameters.

5.1 *BEM Characterization*

In order to characterize the BEM, a linearly polarized signal has been considered as input to the system and, therefore, the incoming voltages into the BEM have the same amplitudes and phases. A broadband noise-like signal has been used as input excitation, accomplished with a noise source (model HP346C) and a passive power divider in order to get into both branches. Using this set-up, shown in Fig. 20, the BEM input power is close to the one delivered by the FEM working in the nominal operation point when the receiver is facing the sky around −59 dBm.

The output powers and the output spectra are measured in the four outputs of the correlation module for each frequency band. Figure 21 shows the output spectral density for the phase-state "0-0" for a white-noise like input signal. This figure shows eight traces, four for each frequency sub-band, where different power levels can be seen. The results for other phase states are analogous, in which the output power levels are interchanged as a result of the different states of the phase switches.

The BEM output power is measured with a power meter for several phase states of both phase-switches, which are controlled by an Arduino board. The Arduino board is programmed to control both phase switches in the BEM independently. One single Arduino board will commutate the phase-switch states of the whole interferometer composed of several BEMs since all the phase-switches of branch#1 in the BEMs are synchronized to one state and the phase-switches of branch#2 to another one. A low switching rate of a few hertz is used for the measurements, which is suitable to demonstrate the BEM performance but higher switching rate will be used in the final instrument in order to overcome the level of $1/f$ noise. The phase state has

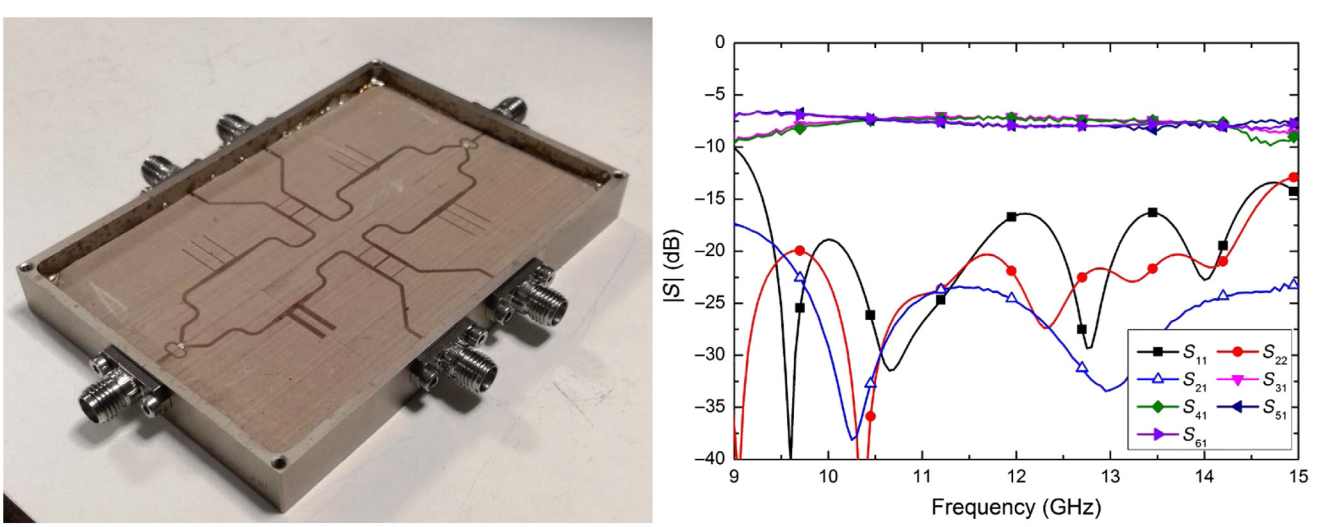

(a) (b)

Fig. 17 (a) Photograph of the 10 to 14 correlation module. (b) Insertion loss, matching, and isolation (S21 parameter) measurements.

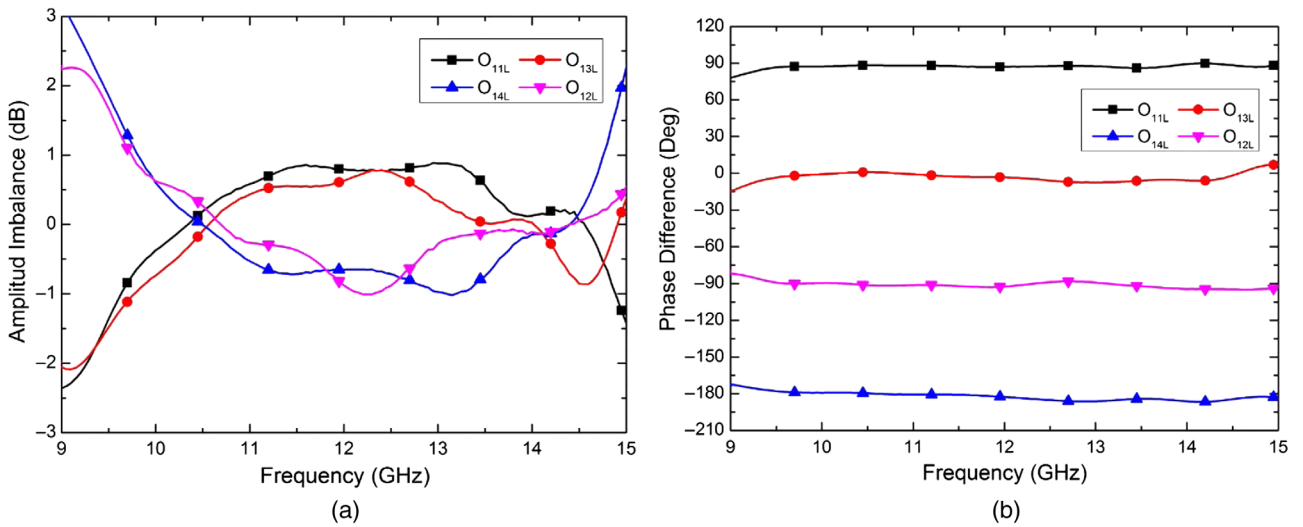

Fig. 18 Measurement results for the correlation module: (a) amplitude difference between outputs and (b) phase difference between outputs.

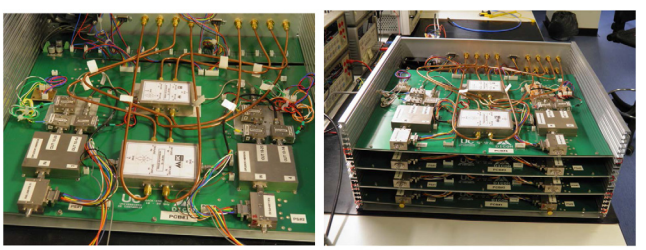

Fig. 19 BEM assembly. (a) One board including the subsystems of two branches. In the foreground the inputs and in the background the eight output connector of one BEM. (b) BEM rack with the four PCBs. In the foreground, the eight inputs, two per receiver.

Fig. 20 View of the BEM rack under characterization with an input noise source.

been swept from 0 deg to 360 deg with 45 deg phase steps, although the phase switch circuit allows steps as low as 5.625 deg. The output powers for both sub-band correlators for the 64 phase states with −59 dBm input power are shown in Fig. 22. Since the individual subsystems in a branch of the receiver could show slight differences in their phase response, related to the one assembled in the other branch of the receiver, both signals are affected for a phase imbalance. Therefore, one of the branches of the BEM is provided with an adjusting phase coaxial element, in order to minimize phase differences between branches. This adjusting phase is slightly different for each sub-

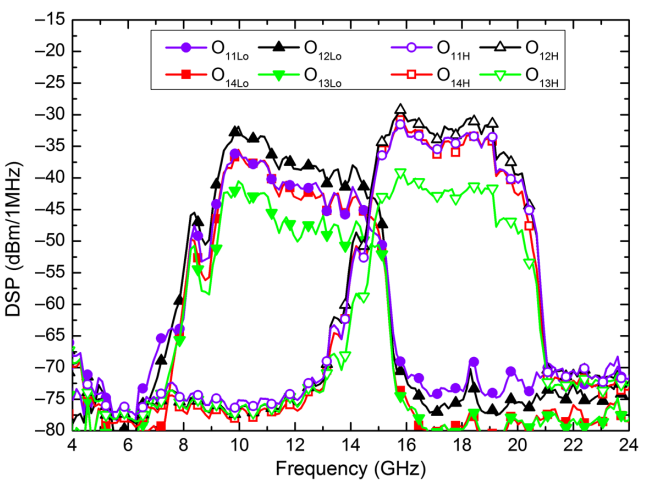

Fig. 21 Output spectral density for the four outputs of the two correlation modules for the phase-state "0-0."

band and hence, it must be necessarily done at the diplexer outputs.

The BEM noise temperature of each sub-band is measured using the Y-factor with the noise source states. The obtained noise temperature is around 287 K. The FEM gain is around 33 dB, so the noise temperature contribution of the BEM to the whole noise temperature receiver is around 0.14 K.

5.2 *Receiver Noise Temperature*

Receiver noise temperature is obtained using the Eq. (13). The vacuum window of the foreseen cryostat and the infrared filter in front of the horn antenna have been considered ideal without contribution to the noise. Therefore, in Eq. (13), gains G_{window} and G_{IRfilter} are equal to 1 and noise temperatures T_{window} and T_{IRfilter} are 0 K. The noise temperature of the passive elements in the FEM is obtained based on the measured insertion loss of each subsystem considering a working ambient temperature of 20 K. The noise temperature values of cryogenic amplifiers and BEM amplifiers are from measurements at 20 and 300 K

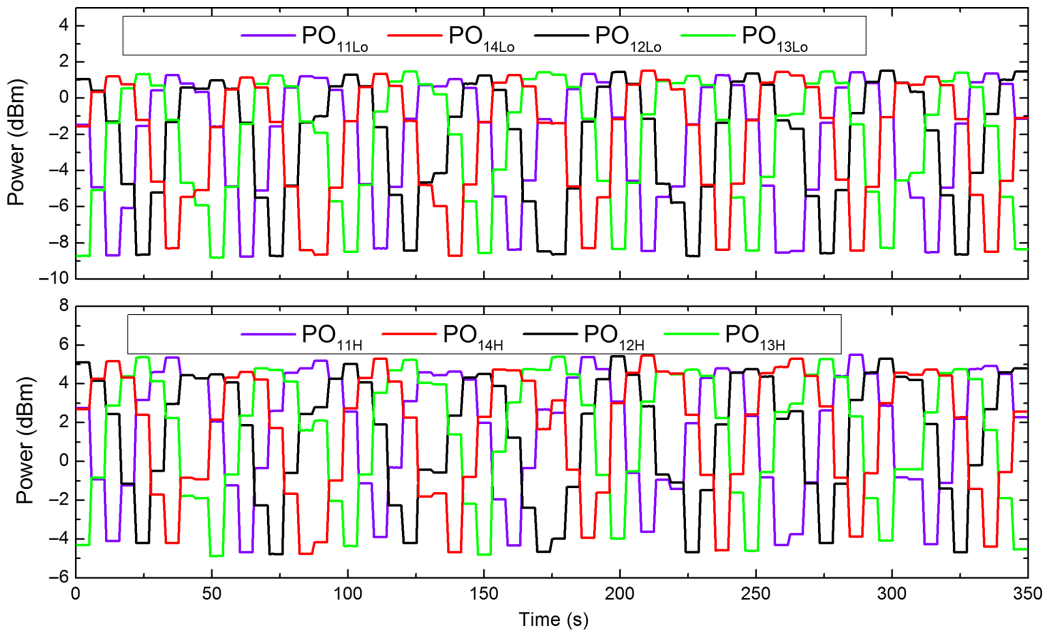

Fig. 22 Output powers for the 64 phase states in both sub-bands: 10 to 14 GHz (Lo) and 16 to 19.5 GHz (H).

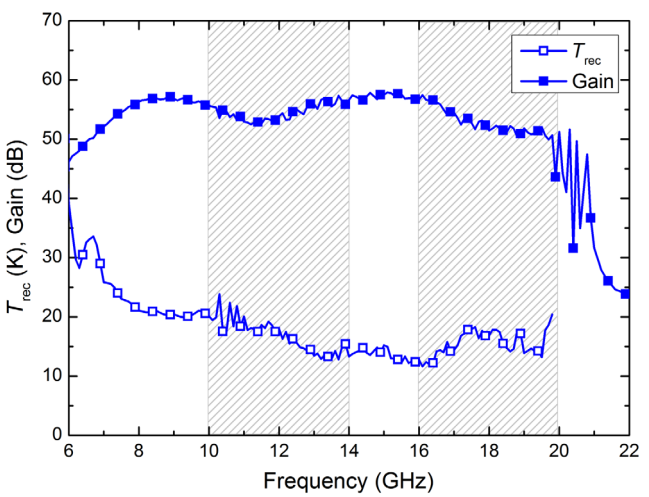

Fig. 23 Receiver noise temperature. Gain including insertion loss of the passive elements and the gains of the cryogenic amplifiers in the FEM, and the gain of the first amplifier in the BEM.

ambient temperatures, respectively. The receiver noise temperature over the frequency of 10 to 19.8 GHz is shown in Fig. 23. The average noise temperature over the whole band is 15.7 K, being 16.4 K, the average temperature from 10 to 14 GHz and 15.6 K from 16 to 19.8 GHz. The gain in Fig. 23 is around 55 dB for the low-frequency band and around 50 dB for the high-frequency band. This gain includes insertion loss of passive elements, gains of the cryogenic amplifier in the FEM and gain of the first amplifier in the BEM. This gain is high enough and the contribution to the noise of the following subsystems in the BEM and the electro-optical correlator is considered negligible.

6 Conclusion

In this paper, the microwave receiver for a 10- to 19.5-GHz interferometer prototype has been presented. The theoretical analysis of the receiver is described in terms of the output powers, which enable the calculation of the Stokes parameters. Several circuits have been specially designed to cover this frequency band, such as cryogenically cooled subsystems of the FEM and the diplexer and microwave correlators in the BEM. This microwave receiver is capable of separating the circularly polarized electromagnetic field components of the incoming signal, as well as to amplify and to separate the whole frequency band into two sub-bands while variable phase shifts between both components are introduced to cancel systematic errors in the postdetection signal processing. The design and individual test results of all the subsystems comprising FEM, such as feedhorn, polarizer, OMT, and cryogenic amplifiers, are presented. Moreover, the design and the measurement results of all the subsystems in the BEM are exhibited. The characterization of the whole BEM has been presented, where the output power and its spectral density have been obtained for several phase switch states in both frequency sub-bands. The receiver noise temperature over the frequency 10 to 19.8 GHz is 15.7 K without the contribution of the cryostat window and IR filter. The presented interferometer, which employs a phase switch step of 5.625 deg, close to a continuous modulation, allows a reduction of the $1/f$ noise as well as an accurate correction of systematic errors. Finally, the described microwave receiver has been integrated with an electro-optical correlator in order to perform interferometry in the frequency bands 10 to 14 GHz and 16 to 19.5 GHz, obtaining synthesized images to characterize the polarization of the CMB measuring Stokes parameters.

Acknowledgments

The authors would like to thank the Spanish Ministry of Economy, Industry, and Competitiveness for financial support provided through the grant ESP2015-70646-C2-2-R. The authors thank Eva Cuerno for her assistance during the assembly of the circuits.

References

1. J. A. Rubiño-Martin et al., "The QUIJOTE-CMB experiment: studying the polarisation of the galactic and cosmological microwave emissions," *Proc. SPIE* **8444**, 84442Y (2012).
2. P.A. R. Ade et al., "Planck 2013 results. XXIII. Isotropy and statistics of the CMB," *Astron. Astrophys.* **571**, A23 (2014).
3. C. Bischoff et al., "The Q/I imaging experiment instrument," *Astrophys. J.* **768**(1), 9 (2013).
4. R. Hoyland et al., "The QUIJOTE TGI," *Proc. SPIE* **9153**, 915332 (2014).
5. P. L. Richards, "Cosmic microwave background experiments—Past, present and future," in *Joint 32nd Int. Conf. Infrared and Millimeter Waves and the 15th Int. Conf. Terahertz Electron.*, pp. 12–15 (2007).
6. B. Aja et al., "Very low-noise differential radiometer at 30 GHz for the PLANCK LFI," *IEEE Trans. Microwave Theory Tech.* **53**(6), 2050–2062 (2005).
7. M. Bersanelli et al., "Planck pre-launch status: design and description of the low frequency instrument," *Astron. Astrophys.* **520**, A4 (2010).
8. N. Aghanim et al., "Planck 2013 results. III. LFI systematic uncertainties," *Astron. Astrophys.* **571**, A3 (2014).
9. J. A. Rubiño-Martin et al. "The QUIJOTE CMB experiment," in *Highlights of Spanish Astrophysics V, Astrophysics and Space Science Proceedings*, Vol. **3**, pp. 127–135, Springer, Berlin, Heidelberg (2010).
10. E. Villa et al., "The thirty gigahertz instrument receiver for the Q-U-I Joint Tenerife experiment: Concept and experimental results," *Rev. Sci. Instrum.* **86**(2), 024702 (2015).
11. E. Villa et al., "Polarimetric receiver in the forty gigahertz band: new instrument for the Q-U-I joint Tenerife experiment," *Exp. Astron.* **45**(1), 127–146 (2018).
12. N. Halverson et al., "DASI: degree angular scale interferometer for imaging anisotropy in the cosmic microwave background," *Proc. SPIE* **3357** (1998).
13. K.-W. Ng, "Complex visibilities of cosmic microwave background anisotropies," *Phys. Rev.* **63**(12), 123001 (2001).
14. M.-T. Chen et al., "AMiBA: broadband heterodyne CMB interferometry," *Astrophys. J.* **694**(2), 1664–1669 (2006).
15. C.-T. Li et al., "AMiBA wideband analog correlator," *Astrophys. J.* **716**(1), 746–757, (2010).
16. C. M. Holler et al., "A 2-20-GHz analog lag correlator for radio interferometry," *IEEE Trans. Instrum. Meas.* **61**, 2253–2261 (2012).
17. C. M. Holler et al., "A 6–12 GHz analogue lag-correlator for radio interferometry," *Astron. Astrophys.* **464**(2), 795–806 (2007).
18. S. J. Melhuish et al., "A 33-GHz interferometer for cosmic microwave background observations on Tenerife," *Mon. Not. R. Astron. Soc.* **305**(2), 399–408 (1999).
19. C. Wang et al., "A compact analog complex cross-correlator for passive millimeter-wave imager," *IEEE Trans. Instrum. Meas.* **66**(11), 2997–3006 (2017).
20. N. R. Price et al., "Linear electro-optic effect applied to a radio astronomy correlator," *Radio Sci.* **31**(2), 451–458 (1996).
21. F. J. Casas et al., "A microwave polarimeter demonstrator for astronomy with near-infra-red up-conversion for optical correlation and detection," *Sensors* **19**(8), 1870 (2019)
22. J. Delabrouille et al., "Exploring cosmic origins with CORE: Survey requirements and mission design," *J. Cosmol. Astropart. Phys.* **2018**, 14–014 (2018).
23. J. D. Kraus, *Radio Astronomy*, 2nd ed, McGraw-Hill, New York (1986).
24. M. Zaldarriaga and U. Seljak, "All-sky analysis of polarization in the microwave background," *Phys. Rev. D* **55**(4), 1830–1840, (1997).
25. T. Y. Otoshi, *Noise Temperature Theory and Applications for Deep Space Communications Antenna Systems*, Artech House, Norwood, Massachusetts (2008).
26. J. Cernicharo, "ATM: a program to compute atmospheric transmission between 0–1000 GHz," Internal Rep. Institut de Radioastronomie Millimétrique (IRAM) (1985).
27. A. Mediavilla et al., "On the octave bandwidth properties of octagonal-shaped waveguide mode transformers," *IEEE Trans. Microwave Theory Tech.* **59**(10), 2447–2451 (2011).
28. J. L. Cano and A. Mediavilla, "Octave bandwidth in-line rectangular waveguide-to-coaxial transition using oversized mode conversion," *Electron. Lett.* **53**(20), 1370–1371 (2017).
29. A. F. Clark et al., "Electrical resistivity of some engineering alloys at low temperatures," *Cryogenics* **10**(4), 295–305 (1970)
30. A. Tribak et al., "Ultra-broadband low axial ratio corrugated quad-ridge polarizer," in *Proc. Eur. Microwave Conf.*, pp. 073–076 (2009).
31. J. L. Cano and A. Mediavilla, "Quasi-octave bandwidth in-phase three-layer platelet orthomode transducer using improved power combiners," *IEEE Microwave Wireless Compon. Lett.* **28**(12), 1086–1088, (2018).
32. J. Bornemann and V. A. Labay, "Ridge waveguide polarizer with finite and stepped-thickness septum," *IEEE Trans. Microwave Theory Tech.* **43**(8), 1782–1787 (1995).
33. W. Zhong et al., "X-band compact septum polarizer design," in *IEEE Int. Conf. Microwave Tech. Comput. Electromag.*, pp. 137–170 (2011).
34. B. Aja et al., "4-12- and 25-34-GHz cryogenic mHEMT MMIC low-noise amplifiers," *IEEE Trans. Microwave Theory Tech.* **60**(12), 4080–4088 (2012).
35. G. Moschetti et al., "Stability investigation of large gate-width metamorphic high electron-mobility transistors at cryogenic temperature," *IEEE Trans. Microwave Theory Tech.* **64**(10), 3139–3150 (2016).
36. E. Villa et al., "Octave bandwidth hybrid-coupled microstrip diplexer for a broadband radio astronomy receiver," *Rev. Sci. Instrum.* **89**(6), 064706 (2018)

Beatriz Aja received her telecommunications engineering and her PhD from the University of Cantabria, Spain, in 1999 and 2007, respectively. From 2008–2012 and 2013–2015, she was an invited scientist with the Fraunhofer IAF, Freiburg, Germany, in a joint collaboration project with the Centro Astronómico de Yebes, Spain. Since 2014, she has been an assistant professor with the Department of Communications Engineering, University of Cantabria. She has been involved the Planck mission and Q-U-I JOint Tenerife CMB experiment.

Luisa de la Fuente received her physics degree and her PhD in electronic engineering from the University of Cantabria, Santander, Spain, in 1991 and 1997, respectively. Currently, she is a lecturer in the Department of Communication Engineering, University of Cantabria. In the last years she has worked in projects focussed on the Development of Radiometers for space applications, like the Planck Mission and on low noise receivers for the QUIJOTE experiment.

Eduardo Artal engineer (1976) and Dr. Engineer in Telecommunication (1982) from the Technical University of Catalonia, Barcelona, Spain. From 1976 to 1990 he was an assistant professor with the same university. From 1979 to 1981 he joined Mier Allende S.A., Barcelona, working on TV and FM radio re-emitters development. Since 1990 he has been a professor at the University of Cantabria in Santander, Spain. His research is on microwave receivers for radio astronomy.

Enrique Villa received his telecommunications engineering, master's and PhD degrees from the University of Cantabria, in 2005, 2008, and 2014, respectively. From 2006 to 2017, he was a researcher with the University of Cantabria, involved in the design of low-noise high-sensitivity broadband microwave receivers for radio astronomy. Since 2018, he has been a researcher with the Instituto de Astrofísica de Canarias, developing microwave radiometers intended for measuring the radiation from biological tissues within the body.

Juan L. Cano received his PhD from the University of Cantabria, Spain, in 2010. He is a researcher at this university, where he collaborates in the design of microwave receivers for radio astronomy and satellite applications. His research interests include design of low-noise amplifiers in MIC and MMIC technologies, both at room and cryogenic temperatures, design of different hardware for feed networks and the development of technologies for efficient subsystems in multipixel microwave cameras.

Angel Mediavilla received his PhD in 1984 from the University of Cantabria, Spain. From 1980 to 1984 he was Ingenieur Stagiere at THOMSON-CSF, France. From 1987 to 1999 he was an associate professor and since 1999 he has been a full professor at University of Cantabria. During more than 41 years he has worked in areas related to microwave semiconductor modelling, high frequency circuit simulation and optimisation, waveguide structures for satellite/RADAR and radio-astronomy subsystems.